

# The low-field density peak in helicon discharges

Francis F. Chen<sup>a)</sup>

*Electrical Engineering Department, University of California, Los Angeles, Los Angeles, California 90095-1597*

(Received 10 December 2002; accepted 21 March 2003)

Although the density  $n$  in helicon discharges increases monotonically with magnetic field  $B$  for  $B$  larger than a few hundred gauss, as expected from theory, a pronounced density peak is often observed at  $B \sim 50$  G or below. A peak in antenna loading is indeed found in computations using a fluid code as long as reflections from an endplate are taken into account. Various tests show that this peak is caused by constructive interference from the reflected wave. This effect can be used in the design of compact helicon plasma injectors. In addition, it can be the cause of density enhancements previously observed using cusped magnetic fields or aperture limiters. © 2003 American Institute of Physics. [DOI: 10.1063/1.1575755]

## I. BACKGROUND

Helicon discharges have drawn interest because they can convert radiofrequency (rf) energy into plasma density more efficiently than other rf plasma sources. In general,  $n$  increases almost linearly with dc magnetic field  $B$ , but this dependence is violated at low  $B$ , where  $n(B)$  has a local peak for  $B$  around 10–50 G and  $n$  of order  $10^{12}$  cm<sup>-3</sup>. This low- $B$  peak was first detected in our earliest experiments on helicons<sup>1</sup> (Fig. 1) and has subsequently been seen in almost all helicon discharges in this range of  $n$  and  $B$ . This effect has also been seen in the downstream plasma created by a 7-tube array of helicon sources<sup>2</sup> (Fig. 2). Though unexplained for over 10 years, this feature has a practical application in rf sources for fabrication of semiconductor circuits, since the low value of  $B$  would make helicon reactors quite economical, and the densities are in a convenient range. No natural frequencies of the plasma match the 13–27 MHz of these experiments at fields between 10 and 100 G. The closest is the lower-hybrid resonance,<sup>3,4</sup> but this would occur at 4500 G under our conditions. A search for resonant phenomena using a helicon code with finite ion mass (Sec. II) yielded only smooth curves in the low- $B$  region. Only when endplates were added to the code did we see the first sign of a low- $B$  effect in the theory. The purpose of this paper is to show that the low- $B$  peak is probably caused by reflection from endplates and therefore can easily be designed into helicon sources used to inject plasma into a processing chamber.

## II. COMPUTATIONS

A low- $B$  peak in plasma loading of an rf antenna is predictable by helicon codes as long as wave reflection from endplates is included. The code used here is the HELIC code of Arnush,<sup>5</sup> which is similar to many other collisional codes<sup>6–11</sup> used for helicon waves in that the plasma is represented by a cold-plasma dielectric tensor. The two-dimensional (2-D) HELIC code treats radial density profiles

and coupling to the most common antennas, but the dc  $B$ -field must be uniform. In the latest version, the antenna can be located at an arbitrary position between endplates, which can be conducting or insulating. The results obtained here should be reproducible by any of the other similar codes with these features.

The starting geometry for the computations is shown in Fig. 3, and variations from this configuration will be studied. The plasma has a radius  $a = 5$  cm, and the antenna is a thin shell of radius 6 cm. The system is bounded by a conducting shell at a large radius of, say, 15 cm. The antenna is a single  $m = 0$  loop located at  $d = 10$  cm from the nearer endplate, which is an insulator. The other end is far away (200 cm) to simulate injection into an unbounded volume. When the  $m = 0$  antenna is replaced by an  $m = 1$  antenna of finite length,  $d$  is the distance from the midplane of the antenna to the endplate. The standard density profile is flat, with a roll-off at the edges, as is often found in experiment. This profile is shown by the heavy solid line in Fig. 4, as compared with parabolic and uniform profiles. Unless otherwise specified, standard conditions are  $n(0) = 10^{12}$  cm<sup>-3</sup> and  $B = 100$  G.

Figure 5 shows the spectrum of energy deposition vs axial wavenumber  $k$  in the standard configuration with  $n = 10^{12}$  cm<sup>-3</sup> on axis and  $B = 50$  G.  $S(k)$  is the plasma response at each  $k$ , and  $P(k)$  is the net absorption including the antenna spectrum. The two peaks correspond to the first two radial modes of  $m = 0$  helicon waves. Figure 6 is the radial distribution of power deposition for the same conditions. A large peak in  $P(r)$  near the periphery due to the Trivelpiece–Gould (TG) mode<sup>5</sup> is seen, as is normal. This peak would be even larger when weighted by  $r$  to account for the solid angle. Figure 7 is the power deposition vs  $z$ , with the insulating endplate at the left. For  $m = 0$  it is seen that  $P(z)$  peaks under the antenna and decays downstream with a scalelength of about 20 cm. The peak would be downstream from the antenna with an  $m = +1$  helical antenna, which launches waves in a preferred direction. The fields to the left of the antenna are enhanced by waves reflected from the endplate.

<sup>a)</sup>Electronic mail: ffchen@ee.ucla.edu

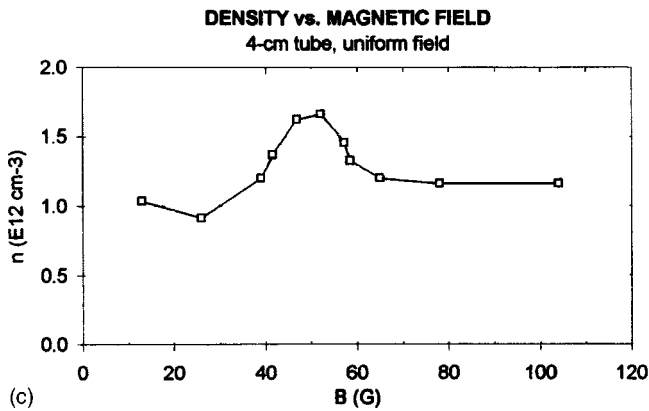
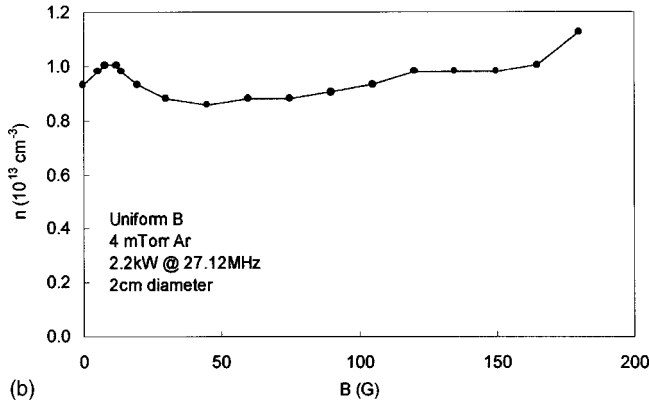
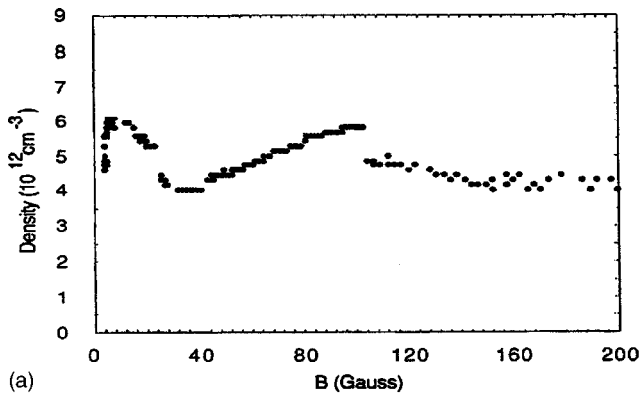


FIG. 1. Low-*B* density peaks observed in 2-cm diam helicon discharges (a) in 1989 and (b) in 1991, and (c) in a 4-cm discharge in 1992 (Ref. 1).

III. RESULTS

The low-*B* peak is clearly seen in computations of the plasma resistance *R*, in ohms, vs *B* at various densities in the standard configuration (Fig. 8). Each point on these curves is computed as follows. For given *k*, a fourth-order differential equation in *r* is solved for the wave fields at that *k*, and integration over the *k*-spectrum gives the total wave field. Integration of **J**•**E** over the plasma volume then gives the plasma loading. As a check, **J**•**E** in the antenna is also calculated; it agrees to within <1%. A clear peak in *R* is seen for  $2 \times 10^{11} < n < 2 \times 10^{12} \text{ cm}^{-3}$ . At higher densities, the peak moves to higher fields and becomes indistinct. This behavior is also observed in the experimental data of Fig. 2(b). In the density range where the peak is distinct, it occurs at a *B*-field increasing linearly with *n*.

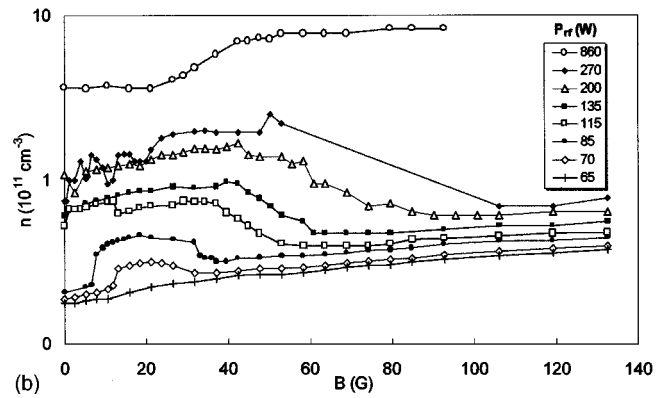
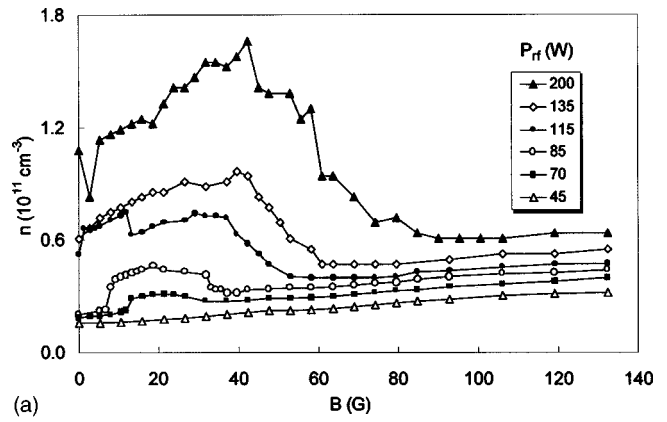


FIG. 2. The low-*B* peak observed in a 7-tube array of helicon sources at (a) low and (b) high *P<sub>rf</sub>* for *m*=0 antennas at 8 mTorr of Ar and 13.56 MHz (Ref. 2). The peak is not seen at higher *P<sub>rf</sub>* (higher density).

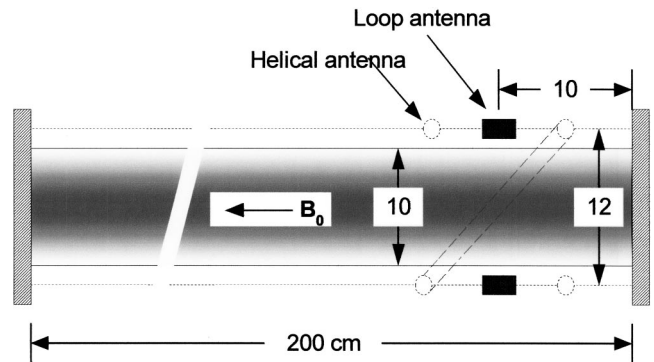


FIG. 3. Starting geometry used in the computations.

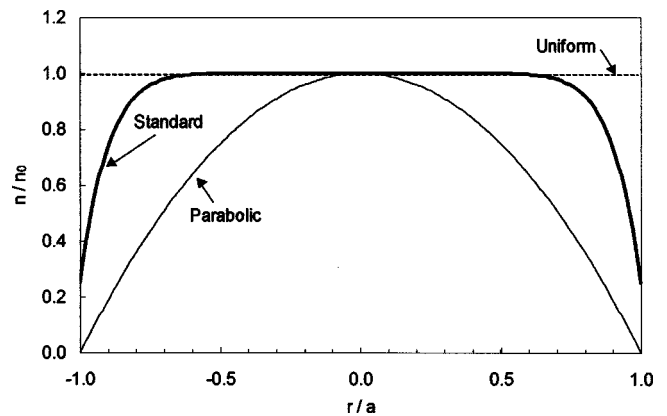


FIG. 4. Radial density profiles assumed in the computations. The heavy curve is the standard one used in most cases.

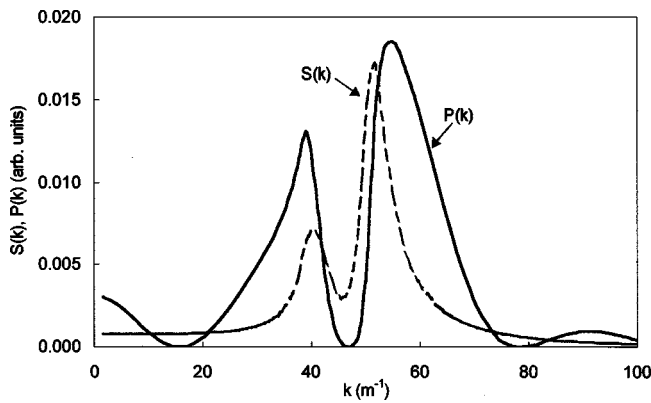


FIG. 5. The  $k$ -spectra of waves excited in the standard configuration.  $S(k)$  is the plasma response, and  $P(k)$  is the convolution of  $S(k)$  with the antenna spectrum.

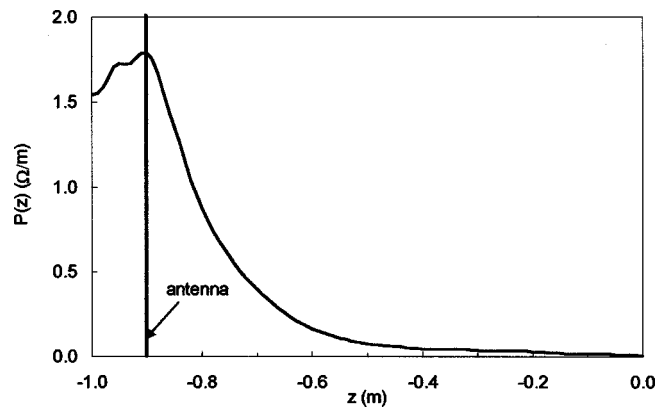


FIG. 7. Energy deposition vs  $z$  (standard configuration). The line is the position of the single loop antenna.

The curves of Fig. 8, however, are not those observed in experiment because they give the plasma resistance, not the density. The latter can be predicted only by codes that include ionization, diffusion, and circuit losses; but a general scaling law is given in Sec. IV. As the loading changes,  $n$  would change at fixed power  $P_{rf}$  and  $B$ , and the plasma would jump to a curve of different  $n$ . An alternative representation is shown in Fig. 9, where  $R$  is plotted against  $n$  for fixed  $B$ . Consider, for instance, the curve at 50 G, where the peak in  $R$  is at  $n_{max}$ , say. If  $n > n_{max}$ , the energy deposition falls, and  $n$  will fall back towards  $n_{max}$ . If  $n < n_{max}$ , the decrease in  $R$  will cause  $n$  to fall further. Thus, only the high- $n$  side of each peak is stable, and the dc value of  $n$  depends on the available power  $P_{rf}$ . When the damping is lowered by decreasing the pressure, the low- $B$  peak becomes sharper, as one would expect.

The cause of the low- $B$  peak is certainly not the lower-hybrid resonance, which occurs at much higher fields. It could be due to a resonance between the helicon and TG waves, which could have similar radial wavelengths at low  $B$ . It could also be due to constructive interference between the forward wave and the wave reflected from the endplate. To distinguish between these two possibilities, several test runs were made. Figure 10 shows the effect of changing the

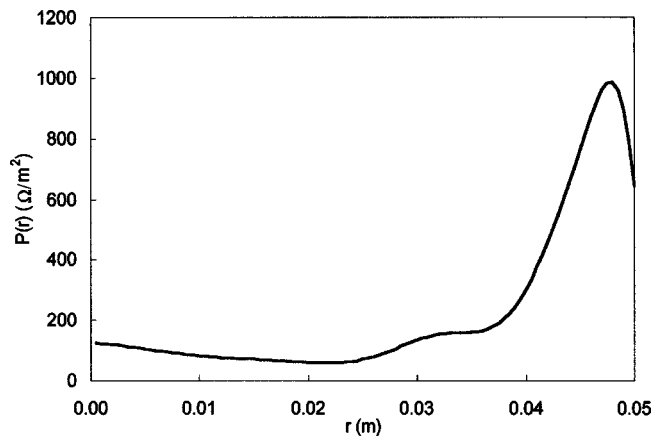


FIG. 6. Energy deposition per unit area vs radius (standard configuration).

density profile. Both the position and the magnitude of the peak are sensitive to  $n(r)$ , suggesting that the TG resonance may be responsible. However, Fig. 11 shows that changing the endplate from insulating to conducting greatly changes the nature of the low- $B$  peak, suggesting that reflection from the end is responsible. Figure 12 provides a definitive test: As the loop antenna is moved from 10 cm to 5 cm in front of the endplate, the low- $B$  peak is changed; and if the plate is removed altogether, the peak no longer exists. There are a number of small peaks which appear in that case, and these could be due to the TG effect.

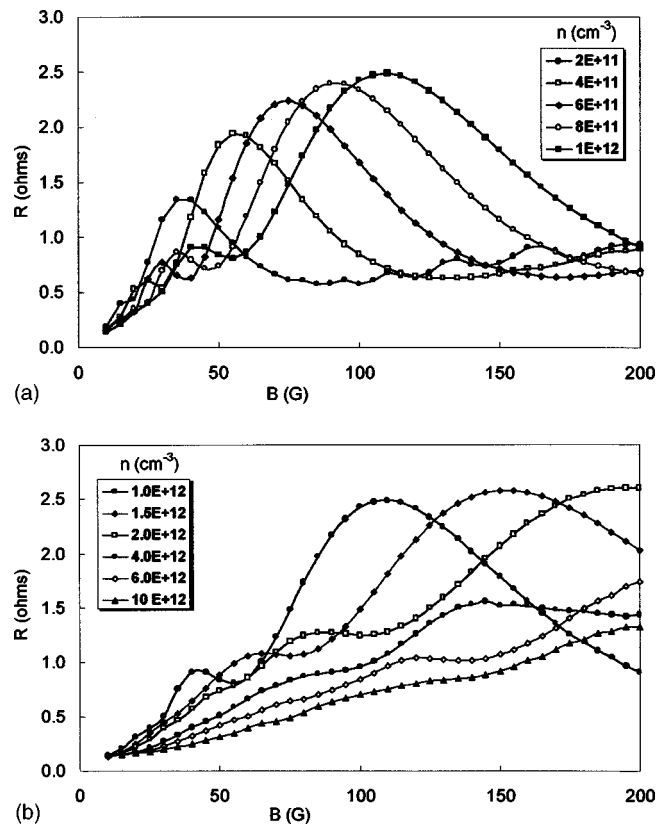


FIG. 8. Plasma loading resistance vs  $B$  for (a) low and (b) high values of  $n$ .

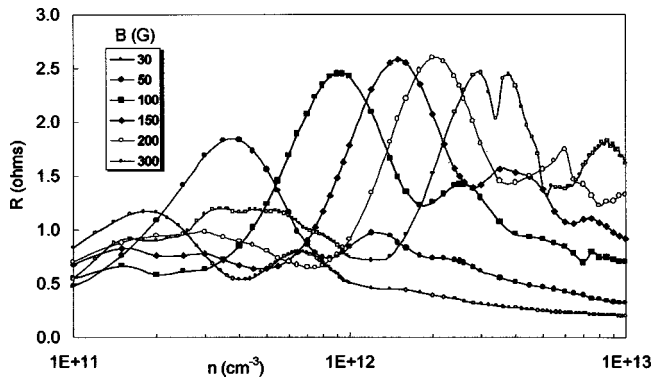


FIG. 9. The low-B peak vs  $n$  at constant  $B$ .

In Fig. 13 we compare the performance of an  $m=0$  loop antenna with those of a half-wavelength helical (HH10)  $m=+1$  antenna and a Nagoya Type III (N3)  $m=\pm 1$  antenna in the low field region. The HH10 antenna is 10 cm long and centered at  $d=10$  cm from the endplate. The low- $B$  peak is barely noticeable with it. This can be understood because this antenna launches only a very weak  $m=-1$  mode towards the endplate, so that the reflected wave is very small. The N3 antenna, on the other hand, is bidirectional, launching strong  $m=+1$  waves in both directions; hence the low- $B$  peak is more noticeable. The directionality of the HH10 antenna is clearly seen in Fig. 14, which shows how the energy deposition is distributed along  $B$ . When  $B$  is reversed so that the  $m=+1$  mode is directed to the left, the peak absorption is at the endplate, and the total loading is not as large as when that mode is directed downstream. Changing the lengths and positions of the  $m=1$  antennas does not improve their low- $B$  performance. It appears that the  $m=0$  loop antenna produces the largest low- $B$  peak.

**IV. RELATION BETWEEN LOADING AND DENSITY**

These computations of plasma resistance are relevant to the density peaks observed because there is a nearly linear relation between them at constant  $P_{rf}$ . The basic principles can be found in textbooks;<sup>12,13</sup> here it will suffice to give a 0-dimensional treatment to show the scaling. Let  $P_{pl}$  be the rf power deposited in the plasma. In steady state, it must

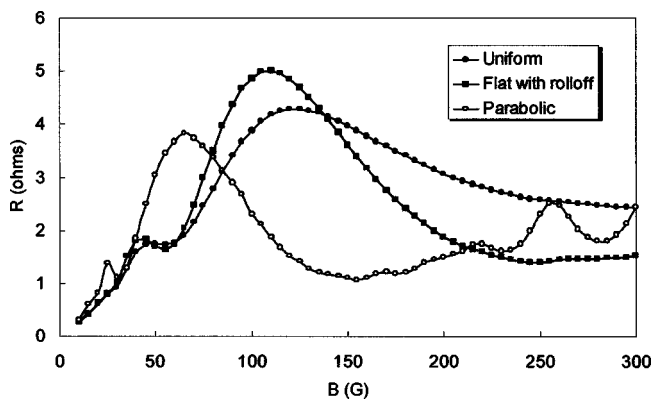


FIG. 10. The low- $B$  peak with different  $n(r)$  under standard conditions: (■) Standard profile, (◆) uniform plasma, and (○) parabolic profile.

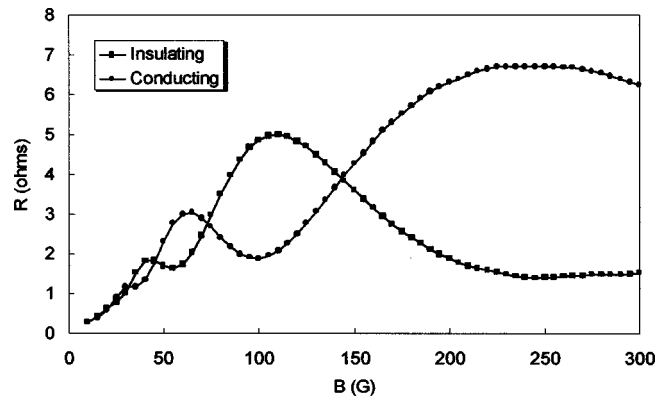


FIG. 11. Effect of the endplate material on the low- $B$  peak.

balance the energy losses. In helicon experiments, electrons are magnetically confined, but argon ions are not. The sign of the radial  $E$ -field suggests that ambipolar diffusion does not occur;<sup>14</sup> rather, the ions diffuse out freely, and the electrons find a way to follow, crossing the  $B$ -field either at the endplates or via high-frequency turbulence. Hence, the total flux of ion-electron pairs out of the plasma is given by the ion flux at the sheath edge, about  $0.5nc_sA$ , where  $A$  is the surface area of the discharge,  $c_s$  is the Bohm velocity (acoustic velocity), and  $\approx 0.5n$  is the density at the sheath edge. Each ion carries with it an energy  $W_i=0.5KT_e+eV_{sh}$ , where  $0.5KT_e$  is its energy entering the sheath, and  $eV_{sh}\approx 4.5$  eV is the sheath drop, so that  $W_i\approx 5KT_e$ . Each electron carries out  $2KT_e$ , including its motion parallel to the wall.<sup>12</sup> More important are the energy losses due to inelastic collisions while the particles are in the plasma. The energy expended in creating each electron-ion pair includes not only the ionization energy but also all the energy lost to line radiation, on average, before the ionization event. This energy, called<sup>12</sup>  $E_c$ , is obtained by summing over all transitions and their probabilities and is a function of  $KT_e$ . This curve can be fit with the following function in the range  $T_{eV}=1-10$  eV, where  $T_{eV}$  is  $KT_e$  in eV:

$$E_c = 22.96 \exp(3.68/T_{eV}^{1.61}). \tag{1}$$

To balance these losses,  $P_{pl}$  must be

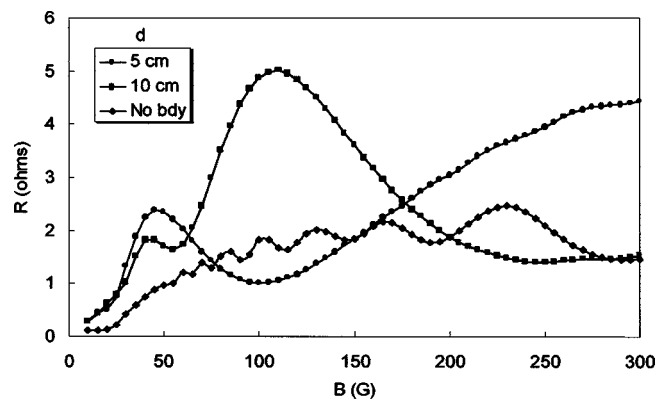


FIG. 12. Effect of antenna position on the low- $B$  peak.

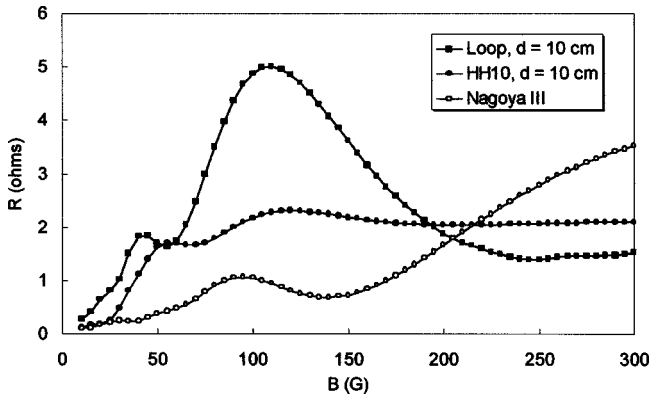


FIG. 13. Comparison of an  $m=0$  loop antenna (■) with  $m=1$  helical (◆) and Nagoya Type III (○) antennas.

$$P_{pl} = 0.5nc_s A_{eff}(W_i + W_e + E_c) = 0.5nc_{s1} A_{eff} T_{eV}^{1/2} (5T_{eV} + 2T_{eV} + E_c), \quad (2)$$

where  $A_{eff}$  is an effective area depending on  $r$  and  $z$  profiles, and  $c_{s1}$  is the acoustic velocity at 1 eV. Using Eq. (1), we can write

$$P_{pl} = 0.5nc_{s1} A_{eff} F(T_e), \quad (3)$$

where

$$F(T_e) = T_{eV}^{1/2} [7T_{eV} + 22.96 \exp(3.68/T_{eV}^{1.61})]. \quad (4)$$

This function is shown in Fig. 15.

The value of  $T_{eV}$  is determined by ionization balance. The total number of ions created per second is

$$\frac{dN}{dt} = V_{eff} n_n n \langle \sigma v \rangle_{ion}, \quad (5)$$

where  $V_{eff}$  is an effective volume,  $n_n$  the neutral density, and  $\langle \sigma v \rangle_{ion}$  the ionization probability (a steep function of  $T_e$ ). The ion loss rate at the Bohm rate is

$$-\frac{dN}{dt} = 0.5nc_s A_{eff}. \quad (6)$$

Equating these yields

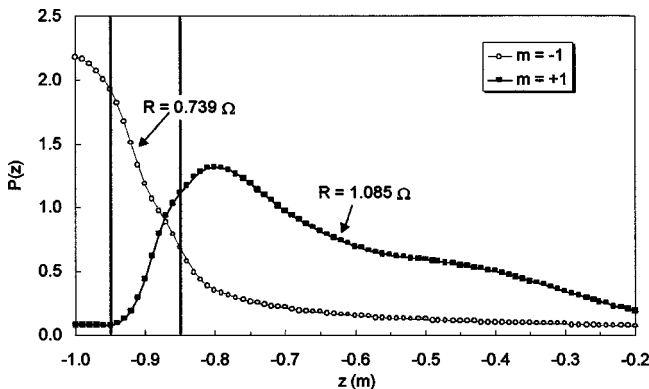


FIG. 14. Axial distribution of absorbed power for the 10-cm half-helical antenna launching the  $m=+1$  mode to the right (■) and to the left (○). The antenna lies between the vertical lines.  $R$  is the plasma resistance in each case.

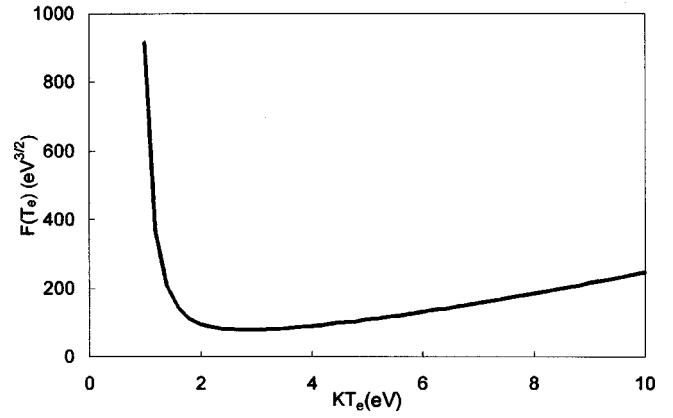


FIG. 15. Function  $F(KT_e)$  describing the energy required to replenish each electron-ion pair.

$$n_n n \langle \sigma v \rangle_{ion} V_{eff} = 0.5nc_s A_{eff}. \quad (7)$$

The plasma density  $n$  cancels out, and for a long, thin cylinder of radius  $a$ ,  $A_{eff}/V_{eff}$  is of order  $2/a$ . We thus have

$$n_n \approx f(T_e)/a, \text{ where } f(T_e) \equiv \frac{c_s}{\langle \sigma v \rangle_{ion}}. \quad (8)$$

After converting  $n_n$  to pressure  $p_0$  in mTorr, this relation is shown in Fig. 16. In the relevant pressure range 3–40 mTorr, it is seen that  $KT_e$  varies from 2.5 to 4 eV. For this range, Fig. 15 shows that  $F(T_e)$  is essentially flat. Equation (3) then shows that  $n$  is proportional to  $P_{pl}$ .

In the experiments,  $P_{rf}$  is kept constant by a matching circuit, but  $P_{pl}$  depends on the circuit losses. Let  $R_c$  be the resistance of the antenna and associated circuitry, and  $R$  the plasma resistance. The power delivered to the plasma is then

$$P_{pl} = P_{rf} R / (R + R_c). \quad (9)$$

From Fig. 9, we see that  $R$  increases from  $\approx 0.5$  to  $\approx 2.5\Omega$ . If  $R_c$  has reasonable values of 0.1 to  $0.5\Omega$ , Eq. (9) predicts that  $P_{pl}$ , and hence  $n$ , will increase between 16% and 66% at the low- $B$  peak. This is comparable to the 10%–50% variations shown in Fig. 1. Exact agreement, of course, cannot be achieved without detailed measurements of  $r$  and  $z$  profiles and of  $R_c$ , and these were not made because there

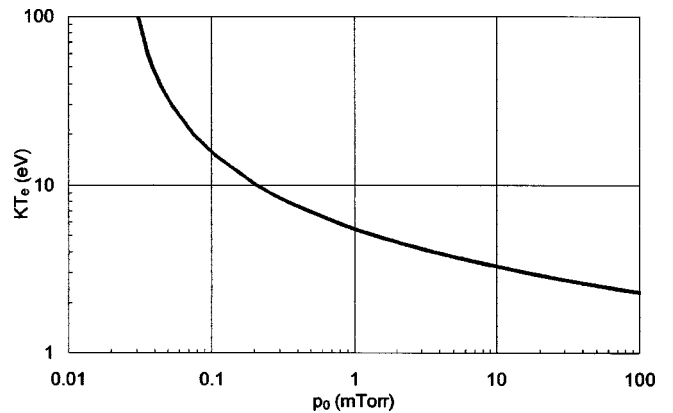


FIG. 16. Relation between  $KT_e$  and  $p_0$  in a low-pressure gas discharge.

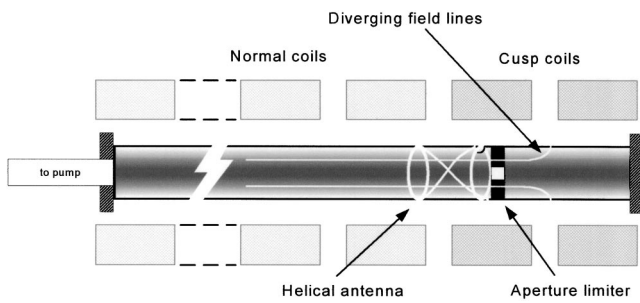


FIG. 17. Schematic of limiter and cusp experiments.

was no theory at the time which called for them. Furthermore, a 2-D code would be necessary to treat these profiles.

**V. APPLICATION TO OTHER DENSITY ENHANCEMENT TECHNIQUES**

At high values of  $n$  and  $B$ , the plasma resistance is so high that essentially all the applied power is delivered to the plasma, and there is no local maximum of  $n(B)$ . Nonetheless, reflection from endplates can explain previously obtained results on density enhancement by aperture limiters and cusped magnetic fields. In 1992, it was found<sup>15</sup> that the plasma density at given pressure and rf power could be doubled by adding an aperture limiter or endplate behind the antenna, or by shaping the magnetic field so that it diverged sharply behind the antenna. These techniques are illustrated in Fig. 17. Tests were made with endplates that were either conducting (carbon) or insulating (BN), with or without a 1-cm diam hole in the center. These plates could be placed downstream of the antenna or within it, where they acted as aperture limiters, or upstream of it, where they acted as endplates. The optimum position was near the upstream end of the antenna (the short end of the vacuum chamber), but the exact position was not critical as long as it was behind the antenna. Density enhancement could also be achieved by reversing the current in the two end coils (Fig. 17) so that the field lines diverged sharply into the chamber wall (as

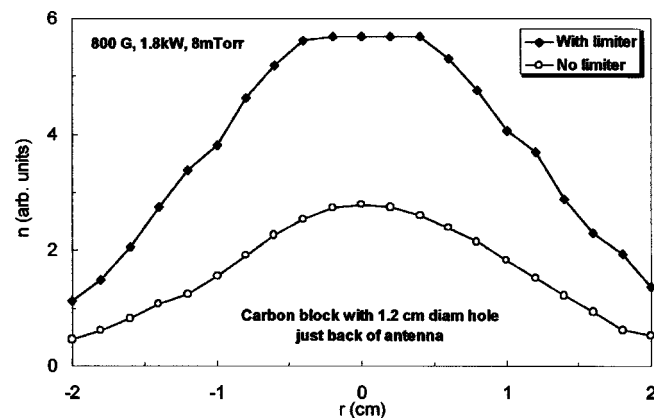


FIG. 18. Radial density profiles with and without an aperture limiter (Ref. 16).

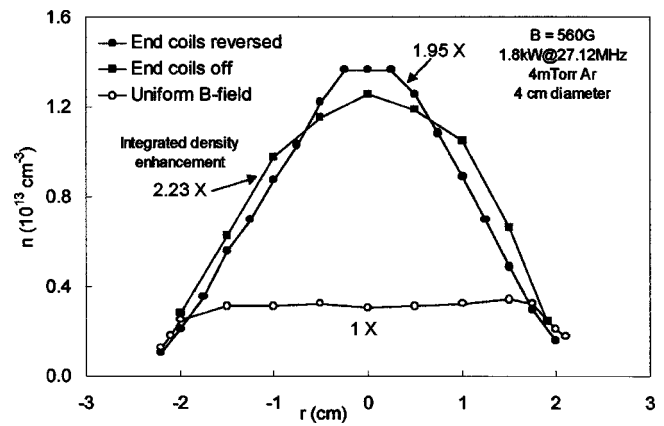


FIG. 19. Radial density profiles in uniform and cusped magnetic fields (Ref. 15).

shown), effectively making it into an insulating endplate. A slight further improvement could be made by applying both techniques together.

The effect of an endplate is illustrated in Fig. 18 for a density above  $10^{13} \text{ cm}^{-3}$  at 800 G,<sup>16</sup> and the effect of a cusped field is shown in Fig. 19.<sup>15</sup> Both techniques are seen to increase  $n$  significantly at the same power. In Fig. 19, curves are shown for different field curvatures with the end coils turned off or reversed. In either case, the density integrated over the tube cross section is increased approximately a factor of two.

When the plasma resistance is computed for the conditions of these experiments, one finds that adding an endplate actually reduces the loading if  $n(r)$  is taken to have the standard shape shown in Fig. 4. It is essential to use the actual, measured  $n(r)$  profiles, which cannot be predicted without an equilibrium code. To see how an endplate affects energy deposition at high fields, we made a HELIC calculation for the parameters of Fig. 18. The result for  $P(z)$  in Fig. 20 shows that the presence of the endplate causes peaks in the collisional absorption and extends the range over which it occurs. The plasma resistance  $R$  increases from 1.21 to 1.97  $\Omega$ .

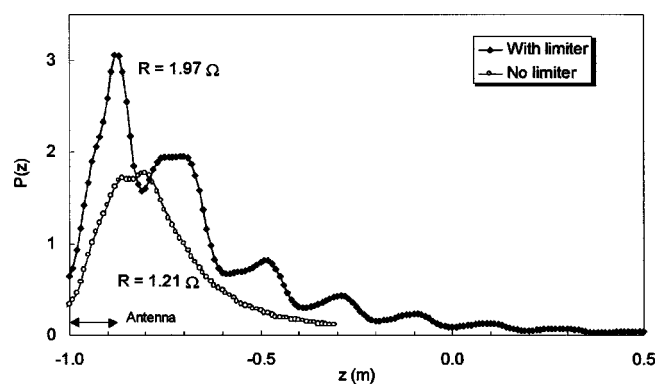


FIG. 20. Energy deposition  $P(z)$  along the  $B$ -field for the conditions of Fig. 18, with and without the aperture limiter. The antenna position is shown at the bottom left.  $R$  is the plasma resistance in each case.

## VI. CONCLUSIONS

Reflection of helicon waves from surfaces behind the antenna can explain two previously unexplained experimental results: the occurrence of a low-field density peak and the factor-of-two density enhancement by endplates and magnetic cusps. These effects can be predicted by cold-plasma fluid codes which include the TG mode and the radial density profile. The low- $B$  peak, in particular, is of interest for design of efficient reactors used in plasma processing.

<sup>1</sup>F. F. Chen, J. Vac. Sci. Technol. A **10**, 1389 (1992).

<sup>2</sup>F. F. Chen, J. D. Evans, and G. R. Tynan, Plasma Sources Sci. Technol. **10**, 236 (2001); J. D. Evans, unpublished, 2001.

<sup>3</sup>S. Yun, S. Cho, G. Tynan, and H. Chang, Phys. Plasmas **8**, 358 (2001).

<sup>4</sup>S. Cho, Phys. Plasmas **7**, 417 (2000).

<sup>5</sup>D. Arnush, Phys. Plasmas **7**, 3042 (2000).

<sup>6</sup>S. Cho and J. G. Kwak, Phys. Plasmas **4**, 4167 (1997).

<sup>7</sup>I. V. Kamenski and G. G. Borg, Comput. Phys. Commun. **113**, 10 (1998).

<sup>8</sup>Y. Mouzouris and J. E. Scharer, Phys. Plasmas **5**, 4253 (1998).

<sup>9</sup>Th. Enk and M. Kraemer, Phys. Plasmas **7**, 4308 (2000).

<sup>10</sup>B. H. Park, N. S. Yoon, and D. I. Choi, IEEE Trans. Plasma Sci. **29**, 502 (2001).

<sup>11</sup>K. P. Shamrai and S. Shinohara, Phys. Plasmas **8**, 4659 (2001).

<sup>12</sup>M. A. Lieberman and A. J. Lichtenberg, *Principles of Plasma Discharges and Materials Processing* (Wiley, New York, 1994).

<sup>13</sup>F. F. Chen and J. P. Chang, *Lecture Notes on Principles of Plasma Processing* (Kluwer/Plenum, New York, 2002).

<sup>14</sup>I. D. Sudit and F. F. Chen, Plasma Sources Sci. Technol. **5**, 43 (1996).

<sup>15</sup>G. Chevalier and F. F. Chen, J. Vac. Sci. Technol. A **11**, 1165 (1993).

<sup>16</sup>I. Sudit, unpublished, 1995.